Maximum Power Point Tracking for Photovoltaic Optimization Using Ripple-Based Extremum Seeking Control

Steven L. Brunton, Clarence W. Rowley, Sanjeev R. Kulkarni, *Fellow, IEEE*, and Charles Clarkson

***Abstract*—This study develops a maximum power point tracking algorithm that optimizes solar array performance and adapts to rapidly varying irradiance conditions. In particular, a novel extremum seeking (ES) controller that utilizes the natural inverter ripple is designed and tested on a simulated solar array with a grid-tied inverter. The new algorithm is benchmarked against the perturb and observe (PO) method using high-variance irradiance data gathered on a rooftop array experiment in Princeton, NJ. The ES controller achieves efficiencies exceeding 99% with transient rise-time to the maximum power point of less than 0.1 s. It is shown that voltage control is more stable than current control and allows for accurate tracking of faster irradiance transients. The limitations of current control are demonstrated in an example. Finally, the effect of capacitor size on the performance of ripple-based ES control is investigated.**

***Index Terms*—Current control, control systems, DC–AC power conversion, extremum seeking control, inverters, optimization methods, photovoltaic power systems.**

I. Introduction

RECENTLY, there has been significant environmental and political motivation to shift domestic power generation to renewable sources such as wind and solar. Solar power is at the forefront of clean, renewable energy, and it is gaining momentum due to advances in solar panel manufacturing and efficiency as well as increasingly volatile fuel costs. Solar power is an attractive option because of the large amount of power available in incident sunlight, particularly in large industrial parks and residential suburbs. However, photovoltaic (PV) solar cells, the most readily available solar technology, operate best on bright days with little or no obstruction to incident sunlight. Frequent overcast days and partial obstructions such as tree limbs or neighboring buildings limit the efficiency and reliability of solar power throughout much of the United States [1]. This study is motivated by the need to optimize solar array performance for rapidly varying environmental conditions, such as those characteristic of New Jersey's climate.

Manuscript received December 14, 2009; revised February 22, 2010, March 8, 2010, March 22, 2010, and April 13, 2010; accepted April 25, 2010. Date of current version September 17, 2010. This work was supported by the New Jersey Commission on Science and Technology. Recommended for publication by Associate Editor K. Ngo.

S. L. Brunton, C. W. Rowley, and S. R. Kulkarni are with the Princeton University, Princeton, NJ 08544 USA (e-mail: sbrunton@princeton.edu; cwrowley@princeton.edu; kulkarni@princeton.edu).

C. Clarkson is with the ITT Geospatial Systems, Rochester, NY 14606 USA (e-mail: chclarks@gmail.com).

Digital Object Identifier 10.1109/TPEL.2010.2049747

Because of the photovoltaic nature of solar panels, the I–V curves depend nonlinearly on temperature and irradiance levels [2], [3]. Therefore, the operating current and voltage, which maximize power output will change with environmental conditions, as shown in Fig. 2. In order to maintain efficient operation despite environmental variations, one approach is to use a maximum power point tracking (MPPT) algorithm to dynamically tune either control current or voltage to the maximum power operating point.

Typically MPPT algorithms are implemented on a solar array using a switching power converter. For example, with a grid-tied inverter, the solar array charges a capacitor, and then current is switched out of the capacitor at a varying duty cycle in order to reconstruct a sinusoidal current, which injects power into the grid. A number of solar power converter architectures are discussed in the literature [4]–[8]. In the majority of power converters, the internal switching mechanism imposes a voltage and current ripple, which is felt by the PV array. Minimizing the magnitude of this ripple has been a major concern, and is achieved by careful (and expensive) choice of the capacitor and inductor.

There are a number of MPPT algorithms for changing environmental conditions [9], [10]. Control algorithms, which do not assume a particular model and are adaptive to changing system parameters, are ideal for a number of reasons including less frequent maintenance and fine-tuning. Adaptive, model-independent algorithms are applicable to a wide range of panel and inverter technologies. A number of "black box" MPPT algorithms such as the perturb and observe (PO) [9] and incremental conductance [2] have been explored in the literature [10].

The PO is a workhorse MPPT algorithm because of its balance between performance and simplicity. In its simplest form, the PO algorithm tracks the MPP by perturbing the control input in a given direction and observing if the output power goes up or down; if the power increases, the perturbation direction is unchanged, and if the power decreases, the direction is reversed. Because the standard PO method uses a fixed perturbation size, it suffers from a performance tradeoff between transient rise time and steady-state performance. PO has also been shown to track in the wrong direction given rapidly varying irradiance [10]. Modified versions of PO have been proposed, for example, by using an adaptive step that is related to $\Delta P/\Delta u$ (where P is power and u is either perturbed voltage or current) [11], or by including rudimentary model assumptions [12].

A promising new MPPT algorithm is the method of extremum seeking (ES) control, which may be closely related to the ripple

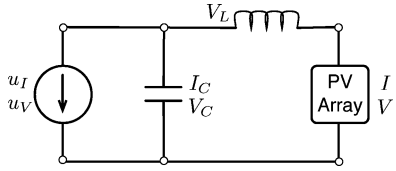

Fig. 1. Schematic of PV array and inverter with LC dynamics. The inverter control variable u is either current or voltage and is controlled by the inverter's switching logic.

correlation control (RCC) and PO methods. The ES method of Krstic [13] offers fast convergence and good steady-state performance with guaranteed stability for a range of parameters. Leyva *et al.* [14] and Bratcu *et al.* [15] implement ES control by injecting an external perturbation signal. The RCC utilizes the natural inverter ripple and corrects the duty cycle of the switching converter in order to set $\dot{P}\dot{I} = 0$, which is a condition for the MPP. The duty cycle is updated using either a discrete comparison, as in PO [16], [21], [22], or using the product of the high-pass-filtered power and control variable, as in ES control [17], [18].

The approach here is to develop an ES controller that utilizes the natural 120-Hz inverter ripple to track the MPP in rapidly varying irradiance conditions. In particular, the ES controller is compared against a well-tuned PO algorithm on high-variance irradiance data measured for use on a solar array on the roof of Princeton's engineering quad. This study also compares the use of voltage and current as control variables and demonstrates limitations of current control for the gradient climb methods. Finally, the effect of capacitor size on ES control is investigated.

II. PV Array Inverter Model

In order to simulate a comparison of various MPPT algorithms, it is necessary to model the array inverter dynamics. Fig. 1 is a schematic of the array inverter system. The block labeled *PV Array* encapsulates all of the dynamics associated with the solar array including the functional dependence of the I–V curves with irradiance G and temperature T. The switching dynamics of the inverter are encapsulated in the block labeled u, and are discussed below. L and C represent the inductor and capacitor, respectively.

A. PV Array Model

The array I–V curve may be written $I = I(V, G, T)$ and is modeled by the lighted diode equations [2], [3]

$$I = I_L - I_{\rm OS}\left[\exp\frac{q}{Ak_BT}(V + IR) - 1\right] \tag{1}$$

$$I_{\rm OS} = I_{\rm OR}\left(\frac{T}{T_R}\right)\exp\left(\frac{qE_G}{Ak_B}\left(\frac{1}{T_R} - \frac{1}{R}\right)\right) \tag{2}$$

$$I_L = \frac{G}{1000}(I_{\rm SC} + K_{T,I}(T - T_R)) \tag{3}$$

where I and V are the same as in Fig. 1, I_L is the light-generated current, $I_{\rm OS}$ is the cell reverse saturation current, and T is the temperature. Because temperature variations are typically much more gradual than irradiance changes, we assume that temperature is constant, $T_{\rm const} = 300$ K, for the remainder of the analysis. Thus, the functional dependence on T is dropped, and

$$V = V(I, G) \triangleq V(I, G, T_{\rm const}) \tag{4}$$

$$I = I(V, G) \triangleq I(V, G, T_{\rm const}) \tag{5}$$

are equivalent representations of the I–V curves for a constant temperature $T_{\rm const}$ and changing irradiance G. Values and definitions of other terms in the equations are given in the Appendix.

Fig. 2 shows the I–V, P–V, and P–I curves for varying irradiance G using the aforementioned equations and parameters. The P–V characteristic curves are more symmetrical about the maximum power input than the P–I curves. Moreover, the maximum power point occurs at a smaller normalized voltage input, giving voltage control larger failure margins.

B. Inverter Model

Applying Kirchoff's law to the circuit in Fig. 1 yields the following relationships:

$$I = u_I + I_C \tag{6}$$

$$u_V \triangleq V_C = -V - V_L \tag{7}$$

where the inverter control variable u is either current u_I, or voltage u_V.

If the inverter control variable is current u_I, the array I–V curve has the form $V = V(I, G)$ and (7) becomes

$$V_C = -V(I, G) - L\frac{dI}{dt} \tag{8}$$

$$\implies \quad -\frac{dV_C}{dt} = \frac{d}{dt}V(I, G) + L\frac{d^2I}{dt^2} \tag{9}$$

$$= \frac{\partial V(I, G)}{\partial I}\frac{dI}{dt} + \frac{\partial V(V, G)}{\partial G}\frac{dG}{dt} + L\frac{d^2I}{dt^2}. \tag{10}$$

Equation (6) and the capacitor equation yield:

$$\frac{dV_C}{dt} = \frac{I_C}{C} \quad \implies \quad \frac{dV_C}{dt} = -\frac{1}{C}(u_I - I). \tag{11}$$

Combining (10) and (11) yields the system dynamics in terms of inverter control current u_I and array current I

$$LC\frac{d^2I}{dt^2} + C\frac{\partial V}{\partial I}\frac{dI}{dt} + I = u_I - C\frac{\partial V}{\partial G}\frac{dG}{dt}. \tag{12}$$

The dynamical system given by (12) represents a forced oscillator with nonlinear damping. The forcing corresponds to the inverter control current u_I as well as the change in I–V curve due to irradiance change, given by $-C(\partial V/\partial G)(dG/dt)$.

To flow 60-Hz ac power into the grid at a given current $\hat{u}_I$, the inverter switches dc current out of a large capacitor. This requires the following inverter control current with a large 120-Hz oscillation

$$u_I = \hat{u}_I\,(1 + \sin(120 \times 2\pi t)). \tag{13}$$

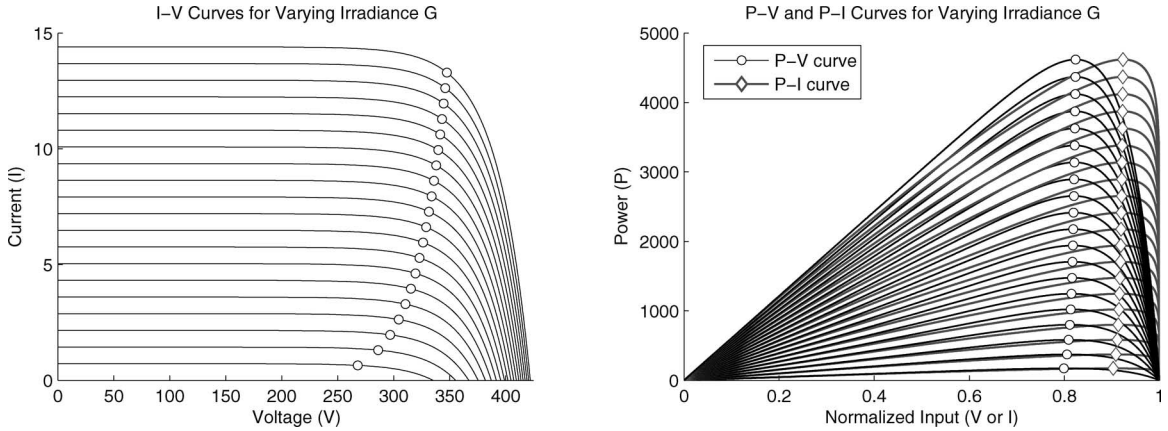

Fig. 2. (Left) I–V curves at several irradiance levels from $G = 50$ W/m^2 to $G = 1000$ W/m^2 (spaced 50 W/m^2 apart). (Right) P–V (black) and P–I (gray) curves plotted against an input variable that is normalized by its maximum allowable value. The maximum power point is labeled as either a black circle or gray diamond.

In practice, the *LC* circuit acts as a low-pass filter between the control current u_I and the array current I so that I experiences a 120-Hz ripple at approximately 3% magnitude

$$I \approx \hat{u}_I \left(1 + 0.03 \sin(120 \times 2\pi t + \varphi)\right). \tag{14}$$

There is also a high-frequency ripple at 20 kHz due to the inverter sampling time; however, this has a negligible effect and is not modeled. For more information on dc–ac power inverters (see Bose [5]).

Similarly, if the inverter control variable is voltage u_V, the array I–V curve has the form $I = I(V, G)$, which yields the following voltage-control dynamics

$$L\frac{\partial I}{\partial V}\dot{V} + V = -u_V - L\frac{\partial I}{\partial G}\dot{G}. \tag{15}$$

Notice that the system type and order of the current-control dynamics (12) and voltage-control dynamics (15) are different. This difference is due to the fact that the control voltage is instantaneously reflected in the capacitor voltage for systems of the form given in Fig. 1.

III. Maximum Power Point Tracking

In the MPPT algorithms implemented in the following, it is assumed that there are current and voltage measurements, which may be multiplied to obtain a power measurement. The control variable is either current or voltage, which are determined by the MPPT algorithm and commanded by the inverter. The algorithms do not require any additional sensors or models to track the MPPT despite exogenous disturbances due to changing irradiance $G(t)$.

Although there are a number of MPPT algorithms that have been developed over the past two decades, this analysis compares a new method, ripple-based ES control, with the standard method, PO. Additionally, an interesting relationship between the existing RCC method and ES control is demonstrated.

The efficiency of each method is given by the formula

$$\eta_{\mathrm{MPPT}}(t) = \frac{\int_0^t P_{\mathrm{actual}}(\tau)d\tau}{\int_0^t P_{\max}(\tau)d\tau} \tag{16}$$

and the transient rise time τ_{rise} is the time it takes the algorithm to reach 90% of the instantaneous maximum power point.

A. Perturb and Observe

The most prevalent MPPT algorithm is PO. The PO repeatedly perturbs the input by a fixed amount in a given direction, and the direction is changed only if a drop in power is detected. Although this algorithm benefits from simplicity, it lacks the speed and adaptability necessary for tracking fast transients in irradiance.

A simple variant of the PO method uses an average power for the comparison step that has been averaged over a number of inverter switching cycles. The effect of this averaged power comparison is a decrease in noise, and also that the perturbation magnitude no longer must exceed that of the natural ripple. This is the version of PO used in this comparison.

Finally, it is possible to construct a PO algorithm with an adaptive step

$$\Delta u_{k+1} = \Delta u_k + \frac{\Delta P_k}{\Delta u_k}. \tag{17}$$

This overcomes the tradeoff between transient rise and steady-state tracking efficiency. However, there are no guaranteed stability conditions for this algorithm, and it is not implemented in this study.

B. ES Control

A new adaptive MPPT algorithm is based on the ES control method. A schematic of the algorithm is shown in Fig. 3. This controller converges at a rate, which is proportional to the slope of the power curve, either P–I or P–V, and has guaranteed stability over a range of system parameters [13], [20]. The algorithm works by adding a perturbation signal $\alpha \sin \omega t$ to the "best guess" for the input $\hat{u}$, which maximizes the quantity of interest, namely, the array output power. The perturbation passes through the system and produces a perturbation in the power. Multiplying the high-pass-filtered control variable u_{hp} (u is u_I or u_V) and high-pass-filtered power P_{hp} results in a demodulated

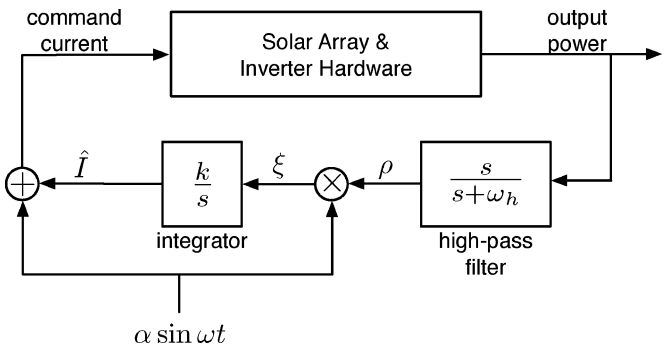

Fig. 3. ES algorithm.

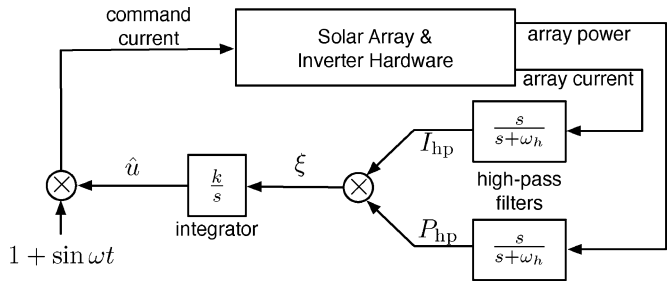

Fig. 4. ES algorithm utilizing natural inverter ripple.

signal ξ, which is positive to the left of the MPP and negative to the right of the MPP. Integrating this signal and adding it to the best guess $\hat{u}$ causes the control variable $\hat{u}$ to adaptively track the MPP. A simple averaging analysis, which assumes constant environmental conditions, shows that the demodulated signal ξ is proportional to the slope of the power curve

$$\xi_{\rm avg} = \frac{\omega}{2\pi}\int_0^{2\pi/\omega} u_{\rm hp} P_{\rm hp} d\tau \tag{18}$$

$$\approx \frac{\partial P}{\partial \hat{u}}(\hat{u}, G)\alpha^2 \sin^2 \omega t. \tag{19}$$

In practice, rather than injecting a sinusoidal control perturbation $\alpha \sin \omega t$, as in the standard ES algorithm, it is convenient to utilize the inverter ripple for the perturbation. Using the control signal in (13), the array current and power will have a small ripple, as in (14). Therefore, the high-pass-filtered array current and power are multiplied, yielding the demodulated signal ξ similar to Fig. 3. A schematic of the new ripple-based ES algorithm is shown in Fig. 4. Details regarding how to tune the ES controller are given in the Appendix.

C. Ripple Correlation Control

RCC utilizes the natural inverter ripple to either perform PO [16], [21], [22], or ES control [17], [18]; RCC has recently been extended to a discrete-time formulation [19]. RCC corrects the duty cycle of the switching converter according to the integral

$$d(t) = k\int \frac{dP}{dt}\frac{dI}{dt}dt \approx k\int P_{\rm hp} I_{\rm hp} dt \tag{20}$$

where $P_{\rm hp}$ and $I_{\rm hp}$ are first-order high-pass-filtered quantities that approximate the derivatives in (20) and k is the integrator gain, similar to Figs. 3 and 4. Using this varying duty cycle, RCC tracks the maximum power point by tracking the equivalent condition $\dot{P}\dot{I} = 0$. In practice, this implementation of RCC is similar to the ES algorithm with first-order high-pass filters. However, RCC lacks the mathematical foundation and careful stability analysis that makes ES attractive for control design. RCC is limited to first-order high-pass filters, which approximate the derivative at low frequencies, whereas ES works also with higher order filters.

IV. Simulated MPPT Comparison

This section summarizes the results of a simulated MPPT comparison between the ES and PO algorithms. The algorithms are tested on rapidly varying irradiance data from measurements on an partially cloudy day. Temperature is assumed constant throughout the simulations because variations in temperature are more gradual than in irradiance. This simplifies the dynamic models (12) and (15). Two sets of algorithm comparisons are simulated, depending on whether voltage or current is controlled by the inverter.

Using the irradiance measurements as an input to the model, both the ES and PO algorithms are tested. The ES model is shown in Fig. 4. Information about the simulated PV system are given in the Appendix.

A. Irradiance Data

Fig. 5 shows irradiance data for two consecutive days in June, 2007. The data were measured on a rooftop of the Engineering Quadrangle at Princeton University. Irradiance is more erratic on the second day because of rapidly moving, scattered cloud cover. The bottom of Fig. 5 provides a detailed view of the irradiance data over a 25-min window between 12:34 and 12:59 A.M., on June 20, 2007 (day 2). This time range is chosen because it includes rapid irradiance changes, and because a short 25-min window makes it possible to see the controller response to individual irradiance changes.

The noisy irradiance measurements are low-pass filtered so that the data are averaged over about 10 s. Because the irradiance sensors are located at points along the array, the measured irradiance responds more quickly to the disturbances than the array. Determining the actual time scales on which irradiance changes affect a solar array will depend on the size and orientation of the array, and should be investigated further. Both unfiltered and low-pass-filtered irradiance sets are used in the simulations below.

B. Voltage Control

Fig. 6 shows the results from a MPPT comparison, where the inverter control variable is voltage. The array power, current and voltage are plotted in time for the ES (black) and PO (light gray) algorithms as well as the true maximum power (dark gray). Both PO and ES command a control voltage, which oscillates closely around the true maximum power voltage (MPV), as seen in the bottom plot. The ES method accurately tracks the maximum

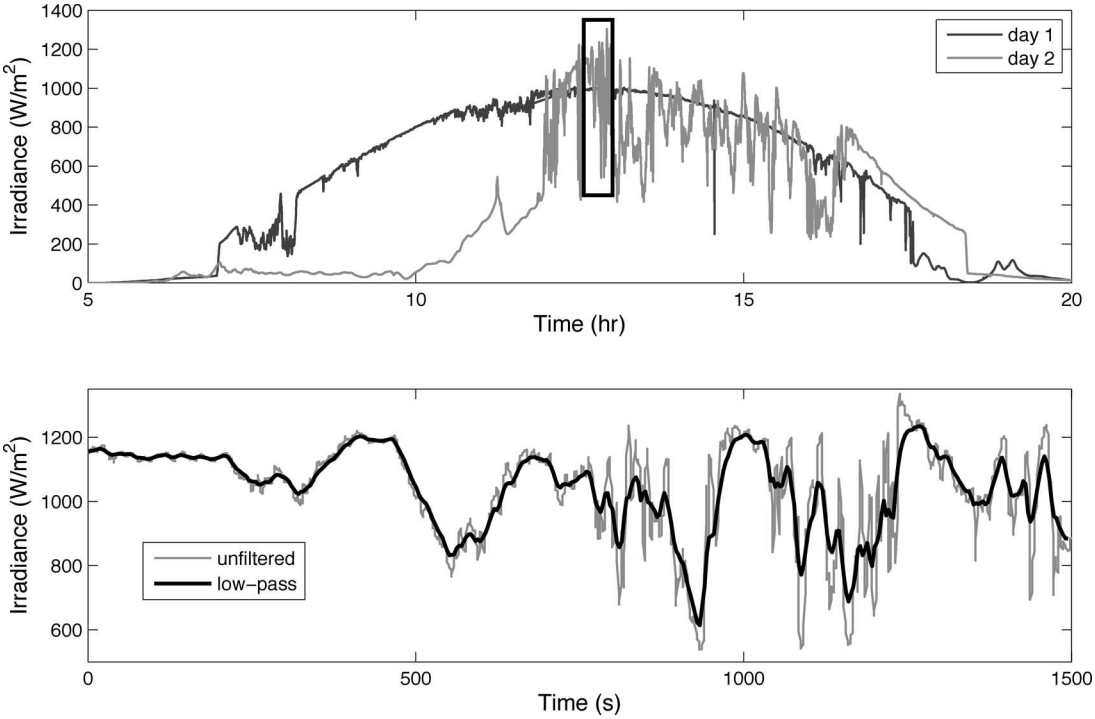

Fig. 5. (top) Irradiance data for two days in June in Princeton, NJ. (bottom) Irradiance data spanning 25 min from 12:34 to 12:59 A.M. on June 20, 2007. Signal is low-pass filtered (black) so that noisy measurements (gray) are averaged over about 10 s.

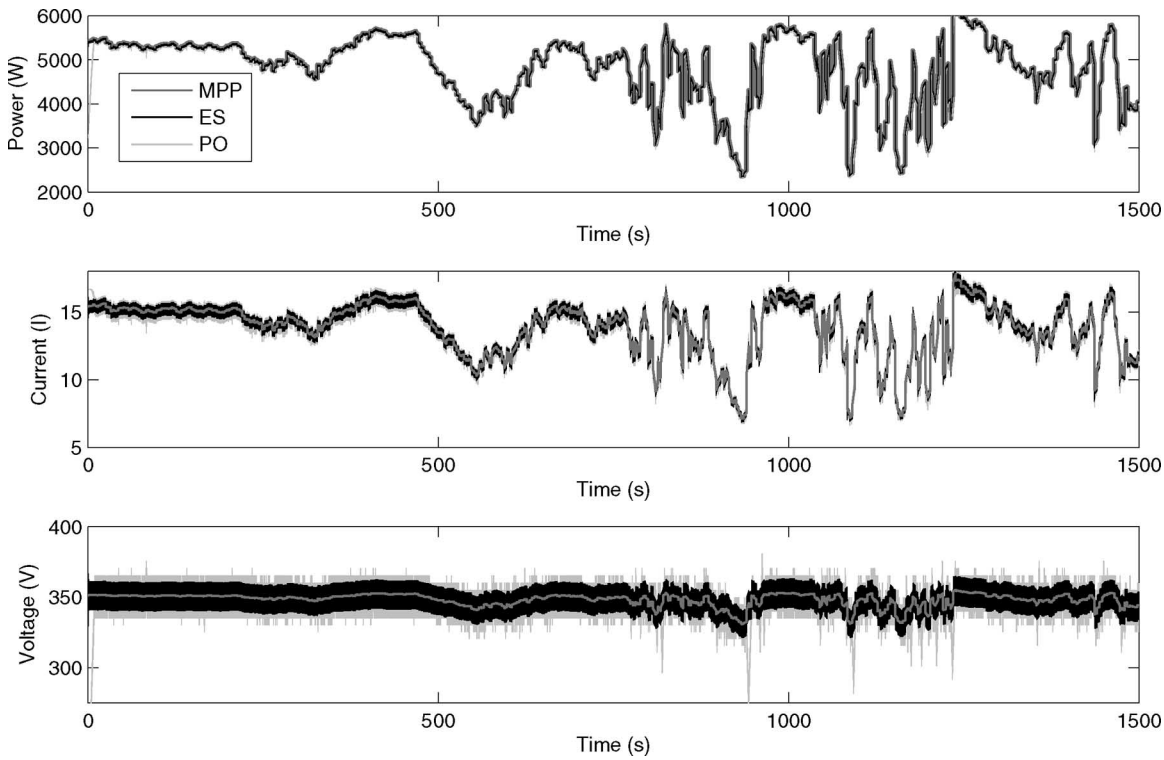

Fig. 6. Comparison of voltage-controlled ES (black) and PO (light gray) controllers on 25 min of unfiltered irradiance data from 12:34–12:59 P.M. (Top) Both controllers track the MPP (dark gray). Commanded array current (middle) and array voltage (bottom) show the large variation in MPI with irradiance and the relative stability of the MPV.

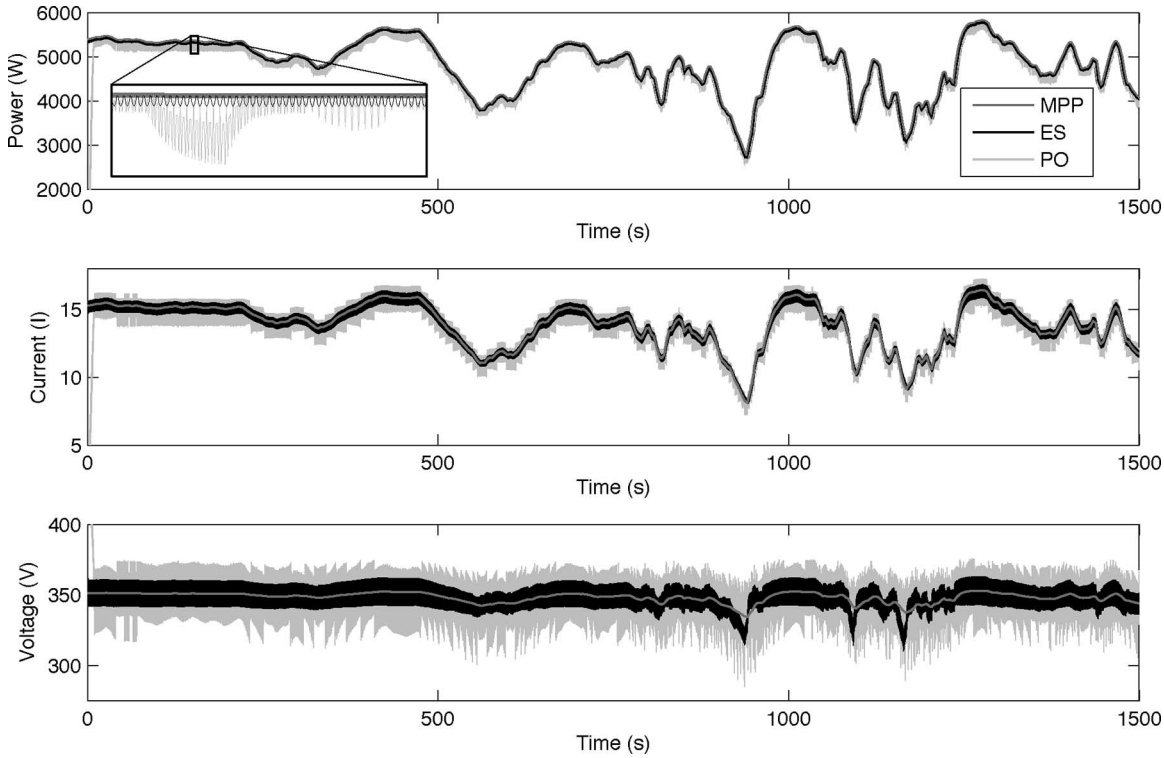

Fig. 7. Comparison of current-controlled ES (black) and PO (light gray) controllers on 25 min of low-pass-filtered irradiance data from 12:34–12:59 P.M. (Top) Both controllers track the MPP (dark gray). Commanded array current (middle) and array voltage (bottom) show the large variation in MPI and the relative stability of the MPV.

power point and rises to the MPP orders of magnitude more rapidly than the PO.

In the voltage-control simulation, each algorithm tracks the MPPT of the unfiltered irradiance measurements. The unfiltered irradiance data vary more rapidly than the filtered data, and therefore, the MPPT is more difficult to track. However, voltage control results in almost perfect MPPT with both ES and PO, achieving efficiencies around 99%. ES has efficiency $\eta_{\rm ES} = 0.9968$ and rises to the MPP in 0.1 s, and PO has efficiency $\eta_{\rm PO} = 0.9939$ and rises to the MPP in 6 s. The inverter hardware uses a 2000-μF capacitor and 1-μH inductor. The PO step size is $\Delta V = 5$ V with 1-kHz sampling. Finally, ES utilizes the natural inverter ripple, which has magnitude of 3%.

C. Current Control

Fig. 7 shows the results from a MPPT comparison, where the inverter control variable is current. The array power, current, and voltage are plotted in time for the ES (black) and PO (light gray) algorithms as well as the true maximum power (dark gray). The ES method commands a control current that oscillates closely around the true maximum power current (MPI), as seen in the middle plot.

In the current-control simulation, each algorithm tracks the MPPT of the low-pass-filtered irradiance data. The current-control dynamics are not easily controllable and fail for the rapid irradiance changes found in the unfiltered data. However, on the low-pass-filtered data, current control with PO and ES admits almost perfect MPPT. ES has efficiency $\eta_{\rm ES} = 0.9963$ with rise time of 0.02 s, and PO has efficiency 0.9898 with rise time of 6.9 s. The step size for PO is $\Delta I = 0.5$ A.

Although both ES and PO track the maximum power point with high efficiency, ES is a more adaptive algorithm. This is seen in Fig. 8, where a number of PO algorithms are compared on an array inverter system with a 2000-μF capacitor. The incremental step is tested using the values $\{0.05, 0.1, 0.25, 0.5, \text{and } 1.0\,\text{A}\}$. The PO step size $\Delta I = 0.5$ A is chosen because this is the only value that doesn't cause the algorithm to fail. For small ΔI, the PO algorithm suffers from slow rise time and insufficient speed to track large irradiance changes, resulting in failure. For the largest step $\Delta I = 1.0$ A, the rise time is faster, but the step size is so large that the oscillation about the MPP reaches the short-circuit current.

In contrast, the ES controller performs well for a large range of ripple magnitudes. To compare the ES algorithm for a number of different ripple magnitudes, it is necessary to vary capacitor size from 250 to 3000 μF; larger capacitors result in smaller ripple, and *vice versa*. The comparison is shown in Fig. 9. As the capacitor size increases, the ES algorithm tracks the MPP with less oscillation due to the decrease in ripple magnitude. However, if the capacitor is too large, the ripple-based control signal is insufficient to track irradiance changes, and the algorithm fails as seen in the case with a 3000-μF capacitor. However, as seen in Table I, ES performs at high efficiencies, even for small capacitor systems with large ripple.

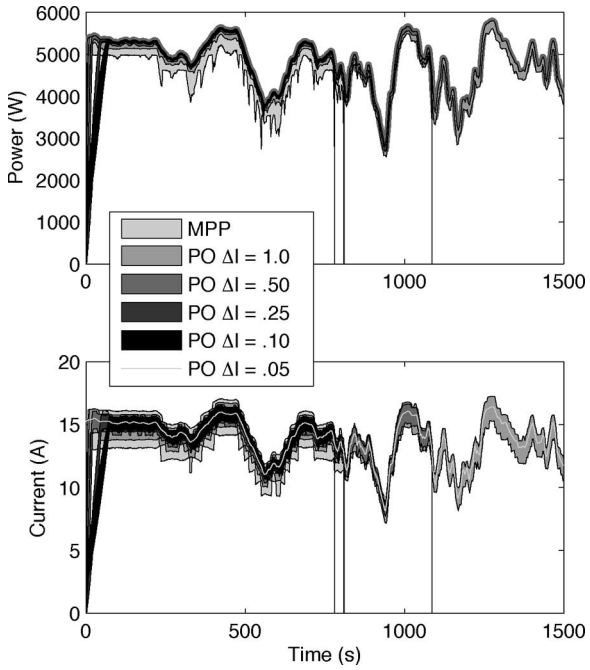

Fig. 8. Comparison of PO controllers, using current control, with varying perturbation step size ΔI. As ΔI is increased, the rise time decreases and oscillations about the MPP increase. The only PO algorithm that is able to track the MPP for every irradiance change is $\Delta I = 0.5$ A.

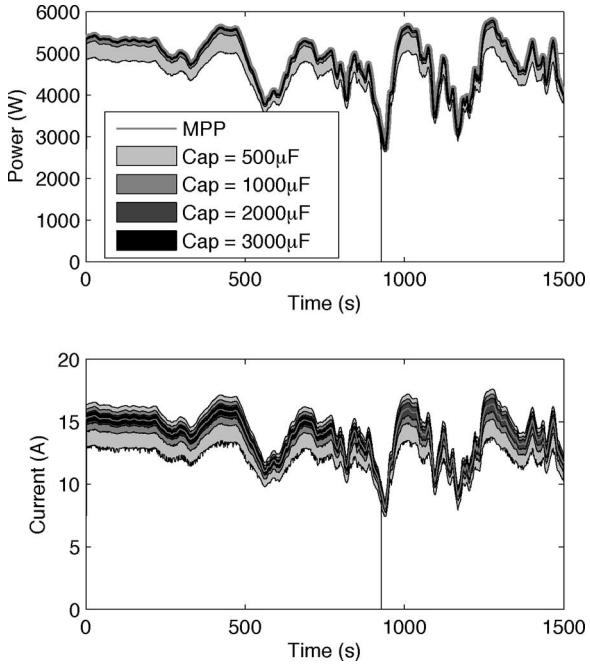

Fig. 9. Comparison of ES controllers, using current control, on inverters with varying capacitor sizes. As capacitor size increases, the ES algorithm tracks the MPP with less oscillation due to the decrease in ripple magnitude. However, if the capacitor is too large, the ripple-based control signal is insufficient to track rapid irradiance changes, and the algorithm fails, as seen when the capacitor is 3000 μF.

TABLE I
ES EFFICIENCY FOR VARYING INVERTER CAPACITOR SIZES

Capacitor Size (μF)	250	500	1000	2000	3000
ES Efficiency (%)	90.71	96.79	98.99	99.63	N/A

D. Limitations of Current Control

As irradiance decreases rapidly, the I–V curve shrinks and the MPV and MPI decrease. If the MPPT algorithm does not track fast enough, the control current or voltage will "fall off" the I–V curve. Fig. 10 shows irradiance plotted against the MPV and MPI as well as the open-circuit voltage and short-circuit current. From these plots, it is clear that voltage control will benefit from much larger margins given rapidly decreasing irradiance. Moreover, if the MPPT algorithm "falls off" the I–V curve, in the case of voltage control, this corresponds to open-circuit, and in the case of current control, this corresponds to short-circuit. Therefore, voltage control not only provides safer margins of operation, but the failure mode is more acceptable than in the case of current control.

Fig. 11 shows the current-control ES algorithm failing to track a rapid irradiance change when the ripple is small because of a large capacitor $C = 3000\,\mu$F. The figure on the left shows the power tracking in time, and the figure on the right shows the corresponding P–I tracking. After a fast rise (shown as 1), the algorithm tracks the MPP with increasing (shown as 2) and decreasing (shown as 3) irradiance until the algorithm fails (shown as 4). Between steps 3 and 4, the control current does not track the MPP quickly enough, and finally the control current falls off the I–V curve, resulting in a short-circuit.

Finally, Fig. 12 shows the high-pass-filtered current $I_{\rm hp}$ and the demodulated product ξ. The signal ξ is integrated into the algorithm's "best guess" of where the MPP current is. At the point of failure, the magnitude of the signal ξ goes to zero. This is explained by the high-pass-filtered current $I_{\rm hp}$, which also goes to zero at the point of failure. Because the current is tracking slowly, as irradiance falls, the current gets closer to the short-circuit current, and therefore, the ripple is constrained by the hard-wired short-circuit current. For this reason, as the current gets closer to $I_{\rm sc}$, the magnitude of the current ripple in the array is constrained and goes to zero, causing the controller to fail.

E. Step Irradiance Changes

It is useful to consider the dynamic response of each method to step changes in irradiance. In addition to representing a worst case scenario, step irradiance changes provide a controlled disturbance on which to compare the tracking performance of each method. Fig. 13 shows the response of each method to step changes in irradiance. The irradiance starts at 200 W/m^2 at time $t = 0$ s and steps up to 1000 W/m^2 at $t = 20$ s. At $t = 40$ s, the irradiance steps back down to 200 W/m^2.

The ES and PO are compared using both current control and voltage control. The current-control methods are initialized with a starting current of 2 A and the voltage-control methods are initialized with a starting voltage of 300 V. Every method is able to track the 800 W/m^2 step-up, although the PO methods have slower response. Only the voltage-control methods are able to track the step-down in irradiance at $t = 40$ s. At $G = 1000$ W/m^2, the current-control methods can only track a step-down of about 40 W/m^2 before short-circuit, as seen in Fig. 10.

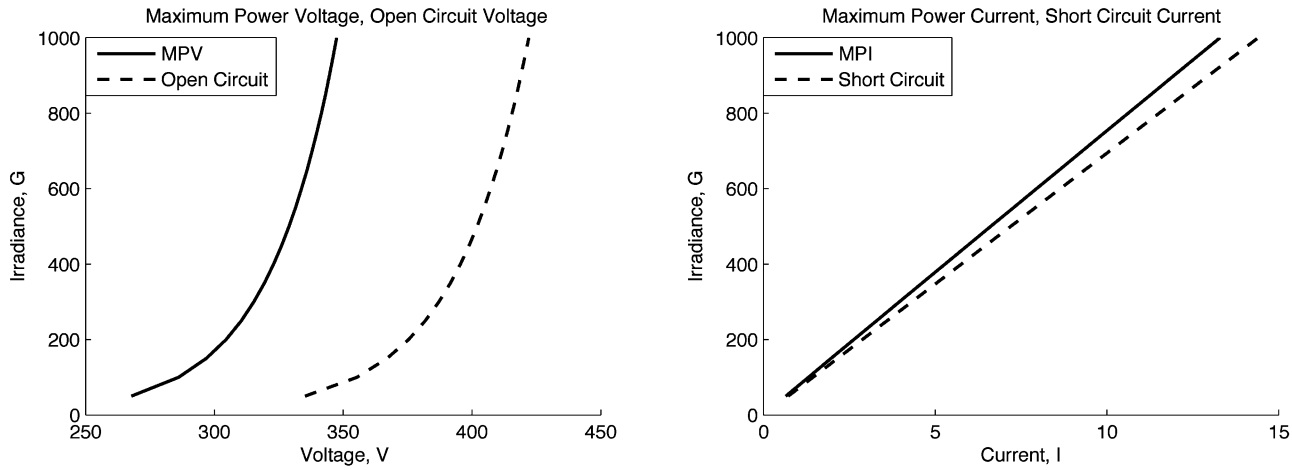

Fig. 10. (Left) MPV (solid) and open-circuit voltage plotted against irradiance G. (Right) MPI (solid) and short-circuit current plotted against irradiance G.

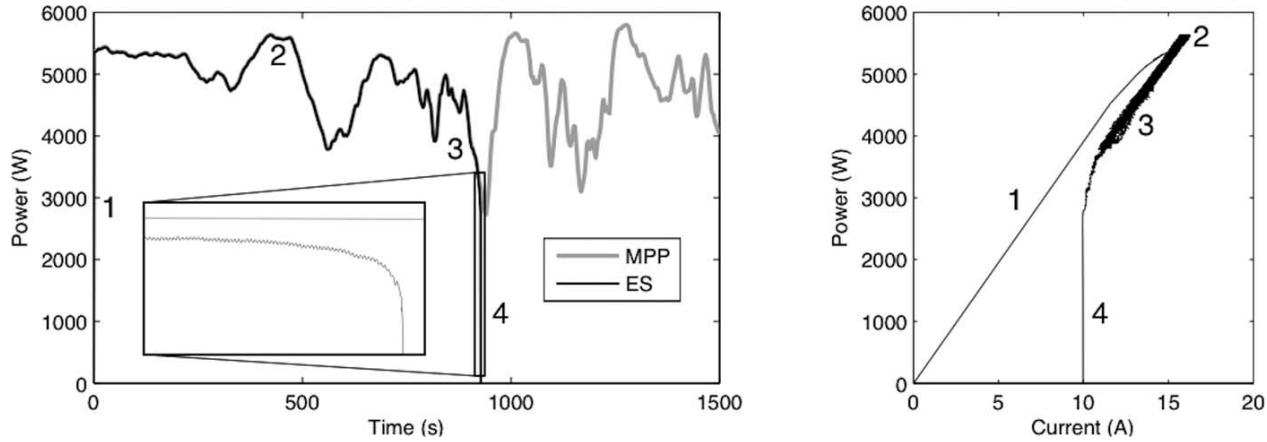

Fig. 11. (Left) Power versus time for maximum power (gray) and ES (black). (Right) Corresponding P–I trace at four stages of tracking: 1—rise, 2—increasing irradiance, 3—decreasing irradiance, and 4—failure.

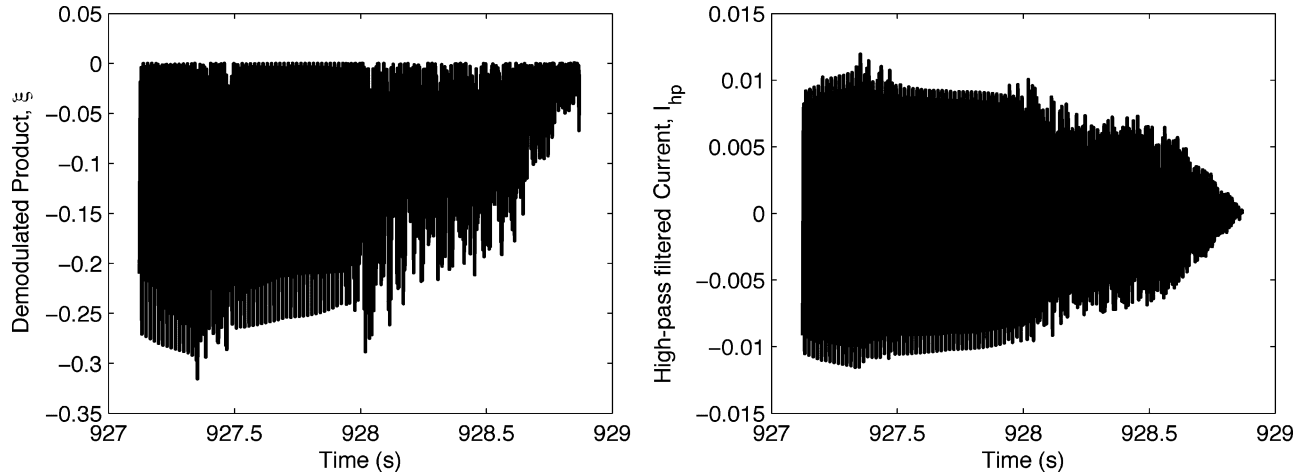

Fig. 12. (Left) Demodulated signal $\xi = I_{\rm hp} \times P_{\rm hp}$. (Right) High-pass-filtered current $I_{\rm hp}$. As irradiance falls, average current $\hat{I}$ nears short-circuit, the ripple is constrained, and the amplitude decreases as the method fails.

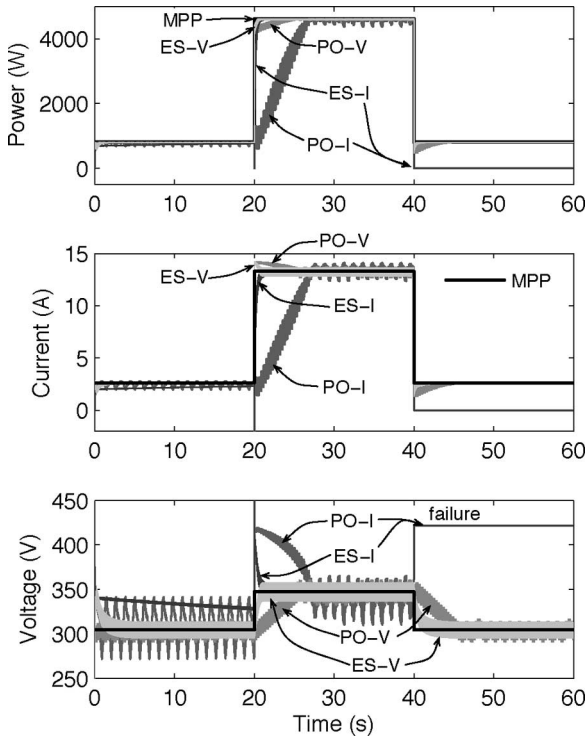

Fig. 13. Comparison of ES and PO using current control (*I*) and voltage control (*V*) on step irradiance changes. The irradiance steps up at $t = 20$ s from 200 W/m^2 to 1000 W/m^2 and steps back down to 200 W/m^2 at $t = 40$ s. Only voltage-control methods track the step-down.

For this reason, both current-control methods fail to track the step-down.

V. Conclusion

A novel ES algorithm that utilizes the natural inverter ripple was tested on a simulated array inverter system. This method was benchmarked against the popular PO method using 25 min of rapidly varying irradiance data taken on June 2007 at Princeton University. The irradiance data represent a worst case scenario for MPPT due to the presence of fast moving, scattered cloud cover. It was shown that ES slightly outperforms PO in total power efficiency, and drastically outperforms in transient rise time to the maximum power point, with two orders of magnitude speed-up. Moreover, ES has guaranteed convergence and stability properties, which are ideal for variable weather conditions and unmodeled dynamics.

The ES and PO algorithms are compared with voltage control and current control. The relative performance of the two algorithms is similar for both voltage and current-control implementations. However, it is shown that the shape of the MPV versus irradiance curve provides significant control benefits including larger margins and an acceptable failure mode. In contrast, the MPI versus irradiance curve is very close to the short-circuit curve, leaving narrow failure margins, which result in short-circuit. The voltage-control implementation is fast enough to handle fully varying irradiance data, while the current-control implementation is only fast enough to track irradiance data that are low-pass filtered over roughly 10 s.

A major result of this study is that the ripple-based ES algorithm has good MPPT performance over a range of inverter capacitor sizes. Typically, the choice of capacitor is expensive because it must be well characterized and large enough to maintain a small ripple. However, because the ES control signal exploits the natural inverter ripple, a smaller capacitor allows the tracking of rapid irradiance changes. Additionally, the ES algorithm may be built using analog components and wrapped around an existing array inverter system with a voltage-control input. This may influence inverter manufacturers to provide a voltage-control input.

Appendix

This appendix contains details of the PV array inverter system, including values and definitions used in the lighted diode equations (1)–(3). Additionally, information related to tuning the ES controller is included.

The system simulated consists of a PV array and grid-tied inverter. The array model consists of three parallel strings, each with seven panels connected in series. Each panel produces approximately 220 W at full irradiance, $G = 1000$ W/m^2. Unless otherwise stated, the inverter hardware uses a 2000-μF capacitor and 1-μH inductor.

Values and definitions of the terms in (1)–(3) are as follows: $T_R = 298$ (reference temperature), $I_{\rm OR} = 2.25e-6$ (reverse saturation current at $T = T_R$), $I_{\rm SC} = 3.2$ (short-circuit current), $E_G = 1.8e-19$ (Silicon bandgap), $A = 1.6$ (ideality factor), $k_B = 1.38e-23$ (Boltzmann's constant), $q = 1.6e-19$ (electronic charge), $R = 0.01$ (resistance), and $K_{T,I} = 0.8$ (short-circuit-current temperature coefficient).

Tuning the ES controller typically involves choice of the perturbation size α and frequency ω as well as the high-pass filter cutoff frequency ω_h and integrator gain k. By utilizing the inverter ripple for the perturbation, α is determined by the capacitor size and ω is given by twice the inverter ac frequency; 60 Hz demodulated is 120 Hz. The cutoff frequency ω_h of the high-pass filter must be slower than the periodic perturbation, and the integrator gain k should be small, as discussed in [13]. In practice, $\omega_h = 750$ rad/s works well, even though it is very close to 120 Hz. The integrator gain k is 0.2 for current control and 0.3 for voltage control, and it is chosen so that the response to transients is fast and stable.

In general, k must be larger, if the capacitor is large, because the magnitude of the ripple-based control signal is smaller for a large capacitor. However, the ES algorithm is adaptive and does not require fine-tuning for excellent performance. In contrast, the step size of the PO method must be carefully chosen to balance the tradeoffs between rise time and steady-state performance, depending on the variability in irradiance.

Acknowledgment

The authors would like to thank M. Holveck, E. Limpaecher, D. Hammell, and S. Banerjee from Princeton Power Systems for gathering irradiance data, as well as for helpful discussions about inverter models. The authors would also like to

thank the anonymous referees for their valuable comments and suggestions.

REFERENCES

[1] V. Quaschning and R. Hanitsch, "Influence of shading on electrical parameters of solar cells," in *Proc. 25th IEEE Conf. Record Photovoltaic Spec. Conf.*, May 1996, pp. 1287–1290.

[2] K. Hussein, I. Muta, T. Hoshino, and M. Osakada, "Maximum photovoltaic power tracking—An algorithm for rapidly changing atmospheric conditions," *IEE Proc.-Generation Transmiss. Distrib.*, vol. 142, pp. 59–64, Jan. 1995.

[3] G. Vachtsevanos and K. Kalaitzakis, "A hybrid photovoltaic simulator for utility interactive studies," *IEEE Trans. Energy Convers.*, vol. EC-2, no. 2, pp. 227–231, Jun. 1987.

[4] B. Bose, P. Szczesny, and R. Steigerwald, "Microcomputer control of a residential photovoltaic power conditioning system," *IEEE Trans. Ind. Appl.*, vol. IA-21, no. 5, pp. 1182–1191, Sep./Oct. 1985.

[5] B. K. Bose, *Modern Power Electronics: Evolution, Technology, and Applications*. New York: IEEE Press, 1992.

[6] R. A. Mastromauro, M. Liserre, T. Kerekes, and A. Dell'Aquila, "A single-phase voltage-controlled grid-connected photovoltaic system with power quality conditioner functionality," *IEEE Trans. Ind. Electron.*, vol. 56, no. 11, pp. 4436–4444, Nov. 2009.

[7] Y. Porasad and H. Hosseinzadeh, "Comparison of voltage control and current control methods in grid connected inverters," *J. Appl. Sci.*, vol. 8, pp. 648–653, 2008.

[8] K. Tse, B. Ho, H. Chung, and S. Hui, "A comparative study of maximum-power-point trackers for photovoltaic panels using switching-frequency modulation scheme," *IEEE Trans. Ind. Electron.*, vol. 51, no. 2, pp. 410–418, Apr. 2004.

[9] D. Hohm and M. Ropp, "Comparative study of maximum power point tracking algorithms," *Progr. Photovoltaics*, vol. 11, pp. 47–62, Jan. 2003.

[10] T. Esram and P. L. Chapman, "Comparison of photovoltaic array maximum power point tracking techniques," *IEEE Trans. Energy Convers.*, vol. 22, no. 2, pp. 439–449, Jun. 2007.

[11] N. Femia, G. Petrone, G. Spagnuolo, and M. Vitelli, "Optimization of perturb and observe maximum power point tracking method," *IEEE Trans. Power Electron.*, vol. 20, no. 4, pp. 963–973, Jul. 2005.

[12] N. Femia, D. Granozio, G. Petrone, G. Spagnuolo, and M. Vitelli, "Predictive & adaptive mppt perturb and observe method," *IEEE Trans. Aerosp. Electron. Syst.*, vol. 43, no. 3, pp. 934–950, Jul. 2007.

[13] M. Krstic and H. Wang, "Stability of extremum seeking feedback for general nonlinear dynamic systems," *Automatica*, vol. 36, pp. 595–601, Apr. 2000.

[14] R. Leyva, C. Alonso, I. Queinnec, A. Cid-Pastor, D. Lagrange, and L. Martinez-Salamero, "Mppt of photovoltaic systems using extremum-seeking control," *IEEE Trans. Aerosp. Electron. Syst.*, vol. 42, no. 1, pp. 249–258, Jan. 2006.

[15] A. I. Bratcu, I. Munteanu, S. Bacha, and B. Raison, "Maximum power point tracking of grid-connected photovoltaic arrays by using extremum seeking control," *CEAI*, vol. 10, pp. 3–12, 2008.

[16] D. Tokushima, M. Uchida, S. Kanbei, H. Ishikawa, and H. Naitoh, "A new mppt control for photovoltaic panels by instantaneous maximum power point tracking," *Electr. Eng. Jpn.*, vol. 157, pp. 73–80, Nov. 2006.

[17] P. Midya, P. Krein, and R. Turnbull, "Dynamic maximum power point tracker for photovoltaic applications," in *Proc. IEEE 27th Annu. Power Electron. Spec. Conf Record, 1996*, Jun., vol. 2, pp. 1710–1716.

[18] T. Esram, J. W. Kimball, P. T Krein, P. L. Chapman, and P. Midya, "Dynamic maximum power point tracking of photovoltaic arrays using ripple correlation control," *IEEE Trans. Power Electron.*, vol. 21, no. 5, pp. 1282–1291, Sep. 2006.

[19] J. W. Kimball and P. T. Krein, "Discrete-time ripple correlation control for maximum power point tracking," *IEEE Trans. Power Electron.*, vol. 23, no. 5, pp. 2353–2362, Sep. 2008.

[20] J. Choi, M. Krstic, K. Ariyur, and J. Lee, "Extremum seeking control for discrete-time systems," *IEEE Trans. Automat. Control*, vol. 47, no. 2, pp. 318–323, Feb. 2002.

[21] Y. H. Lim and D. Hamill, "Simple maximum power point tracker for photovoltaic arrays," *Electron. Lett.*, vol. 36, no. 11, pp. 997–999, May 2000.

[22] Y. H. Lim and D. Hamill, "Synthesis, simulation and experimental verification of a maximum power point tracker from nonlinear dynamics," in *Proc. IEEE 32nd Annu. Power Electron. Spec. Conf., 2001*, vol. 1, pp. 199–204.

Steven L. Brunton received the B.S. degree in mathematics (with a minor) in control and dynamical systems from the California Institute of Technology, Pasadena, in 2006. He is currently working toward the Ph.D. degree in mechanical and aerospace engineering at Princeton University, Princeton, NJ.

His research interests include modeling and control of unsteady aerodynamics, as well as topics in adaptive control and nonlinear dynamical systems.

Mr. Brunton is the recipient of a Gordon Wu Fellowship Award.

Clarence W. Rowley received the B.S.E. degree in mechanical and aerospace engineering from Princeton University, Princeton, NJ, in 1995, and the M.S. and Ph.D. degrees in mechanical engineering from the California Institute of Technology, Pasadena, in 1996 and 2001, respectively.

He joined the faculty of Princeton University in 2001, and is currently an Associate Professor of mechanical and aerospace engineering, and an affiliated Faculty Member with the Program in Applied and Computational Mathematics. His research interests include modeling and control of high-dimensional systems such as fluid flows.

Dr. Rowley is the recipient of the National Science Foundation CAREER Award and the Air Force Office of Scientific Research (AFOSR) Young Investigator Award.

Sanjeev R. Kulkarni (F'04) received the B.S. degree in mathematics, B.S. degree in electrical engineering, and M.S. degree in mathematics from Clarkson University, Ptsdam, NY, in 1983, 1984, and 1985, respectively, the M.S. degree in electrical engineering from Stanford University, Stanford, CA, in 1985, and the Ph.D. degree in electrical engineering from the Massachusetts Institute of Technology (MIT), Cambridge, in 1991.

From 1985 to 1991, he was a Member of the Technical Staff in MIT Lincoln Laboratory. Since 1991, he has been at Princeton University, where he is currently a Professor of electrical engineering. He was a Research Fellow at Australian National University during January 1996, with Susquehanna International Group during 1998, and with Flarion Technologies during summer 2001. His research interests include statistical pattern recognition, nonparametric statistics, learning and adaptive systems, information theory, wireless networks, and image/video processing.

Prof. Kulkarni received the Army Research Office Young Investigator Award in 1992, the National Science Foundation Young Investigator Award in 1994, and a number of teaching awards at Princeton University. He was an Associate Editor for the IEEE TRANSACTIONS ON INFORMATION THEORY.

Charles Clarkson received the B.S.E. degree (with a certificate in engineering physics) in electrical and computer engineering from Princeton University, Princeton, NJ, in 2007, and the M.S. degree in electrical engineering from the University of Rochester, Rochester, NY, in 2009.

Since 2009, he has been at ITT Geospatial Systems Division, Rochester, NY, where he is involved in designing focal planes and associated electronics.